Nano Energy 53 (2018) 808–816

Contents lists available at ScienceDirect

Nano Energy

journal homepage: www.elsevier.com/locate/nanoen

Full paper

# Liquid-phase exfoliated ultrathin Bi nanosheets: Uncovering the origins of enhanced electrocatalytic $CO_2$ reduction on two-dimensional metal nanostructure

Wenjun Zhang[a], Yi Hu[a], Lianbo Ma[a], Guoyin Zhu[a], Peiyang Zhao[a], Xiaolan Xue[a], Renpeng Chen[a], Songyuan Yang[a], Jing Ma[a], Jie Liu[a,b], Zhong Jin[a,*]

[a] Key Laboratory of Mesoscopic Chemistry of MOE, School of Chemistry and Chemical Engineering, Nanjing University, Nanjing, Jiangsu 210023, China
[b] Department of Chemistry, Duke University, Durham, NC 27708, USA

ARTICLE INFO

*Keywords:*
Electrochemical $CO_2$ reduction
Liquid-phase exfoliation
Bismuth nanosheets
Formate
Edge sites

ABSTRACT

Electrochemical $CO_2$ reduction has been considered as a promising route for renewable energy storage and carbon-neutral energy cycle. However, the selectivity and stability of electrocatalysts for $CO_2$ reduction need to be improved. Two-dimensional (2D) layered electrocatalysts with high conductivity and abundant active sites have been considered as good candidates for $CO_2$ reduction. Herein, we propose a liquid-exfoliation strategy to prepare ultrathin 2D bismuth (Bi) nanosheets towards efficient electrocatalytic $CO_2$ conversion. Compared with bulk Bi, the increased edge sites on ultrathin Bi nanosheets played a vital role in $CO_2$ adsorption and reaction kinetics, significantly facilitating $CO_2$-to-formate ($HCOOH/HCOO^-$) conversion. Through density functional theory (DFT) calculation, we found that the *OCOH formation step tended to occur on edge sites rather than on facet sites, as confirmed by the lower Gibbs free energies. Benefited from the high conductivity and rich edge sites, Bi nanosheets exhibited a Faradaic efficiency of 86.0% for formate production and a high current density of 16.5 mA $cm^{-2}$ at − 1.1 V (*vs.* RHE), much superior to bulk Bi. Moreover, the Bi nanosheets could maintain well-preserved catalytic activity after long-term testing for over consecutive 10 h. We hope this study may provide new insights for the fabrication of novel 2D nanostructured metals for highly-efficient and long-life electrocatalytic $CO_2$ conversion.

## 1. Introduction

The unrestrained exploit of fossil fuel and excess $CO_2$ emission have been increasingly deteriorated, posing a serious threat of global warming [1,2]. To achieve a carbon-neutral energy cycle, advanced $CO_2$ fixation technologies are imperatively required, but very hard to be achieved, since $CO_2$ is a thermodynamically stable molecule with the highest oxidation state of carbon [3,4]. In recent years, electrochemical $CO_2$ reduction reaction ($CO_2RR$) has attracted tremendous attention as a promising route for $CO_2$ fixation and conversion into high value-added carbonaceous compounds [5–7]. Especially, formate ($HCOOH/HCOO^-$) was regarded as a suitable candidate for using in hydrogen carrier and HCOOH fuel cells [8,9], which possesses the prominent merits of easy storage and high safety. However, the application of large-scale $CO_2RR$ system was hindered by poor catalytic performance, excessive overpotential and low energy conversion efficiency [10–12]. Therefore, the rational design and preparation of highly-efficient electrocatalysts are urgently needed to alleviate these problems.

As mentioned in our previous review [13], some transition metals (such as Pd, In, Sn, Hg, Pb, *etc.)* with $d^{10}$ electronic configuration have been listed in the same class for selective formate generation, owing to their weak adsorption of $CO_2^{\cdot-}$ intermediates. Nevertheless, the exploitation of an electrocatalyst that meets all of the practical demands, including facile synthesis, environmental friendliness, high safety and low cost, still has a long way to go [14]. With the earth-abundant and environmental benign characteristics [15], Bismuth (Bi), as a main-group metal, was found to be a notoriously poor material for the hydrogen evolution reaction (HER) [16]. Rosenthal et al. employed Bi-based compounds and surface-modified Bi nanoparticles for $CO_2RR$ in acetonitrile (MeCN) with ionic liquid (IL) as the supporting electrolyte, and CO was found to be the main product [17–19]. At a moderate potential, electrodeposited Bi exhibited high Faradaic efficiency for CO production, owing to the strong stabilization of $CO_2^{\cdot-}$ intermediates by imidazolium cations. CO, as a primary component of syngas, was a key

* Corresponding author.
*E-mail address:* zhongjin@nju.edu.cn (Z. Jin).

https://doi.org/10.1016/j.nanoen.2018.09.053
Received 22 July 2018; Received in revised form 18 September 2018; Accepted 20 September 2018
Available online 21 September 2018

feedstock to produce olefins *via* Fischer-Tropsch technology [20]. However, the decomposition of IL at high voltages was intractable to solve. Compared to aqueous systems, the lower stability and higher cost of Bi-based catalysts in organic media hampered their application in $CO_2$RR.

It has been revealed that the limited number of active sites and poor intrinsic activity of bulk electrocatalysts may severely affect the catalytic performances [21,22]. Recently, two-dimensional (2D) materials with abundant active sites and high conductivity have been extensively studied as potential electrocatalysts, which hold a key to enhanced $CO_2$RR activity [23–26]. Theoretically, Bi atomic layers, with the rhombohedral structure composed of puckered six-membered rings of Bi atoms, are stacked in a similar way to black phosphorus [27]. The laminar characteristics of Bi make it possible to form single- or few-layer nanosheets *via* exfoliation. The 2D nanostructures could provide enhanced electrochemical surface area (ECSA) and far more active sites than bulk materials, contributing to the catalytic performance for $CO_2$ fixation.

Following this line of thought, here we propose an ideal model for the scalable preparation of ultrathin Bi nanosheets *via* liquid-phase exfoliation of bulk Bi in an isopropanol (IPA) solution of NaOH. The Bi nanosheets have the merits of ultrathin feature, high electrical conductivity and large ECSA, resulting in preferable $CO_2$ adsorption and rapid electron transfer. Notably, both experimental and theoretical results reveal that the rich edge sites on Bi nanosheets can efficiently facilitate the crucial *OCOH formation step for selective formate production. In result, the Bi nanosheets exhibited high Faradaic efficiency, moderate overpotential and good long-term stability for formate generation in aqueous media, showing very competitive performance among the existing representative electrocatalysts (Table S1) [28–35].

## 2. Experimental section

### 2.1. Chemicals

Isopropanol alcohol (IPA), sodium hydroxide (NaOH), potassium bicarbonate ($KHCO_3$), sodium formate ($HCOONa{\cdot}2H_2O$, 99.99%) and N-methyl pyrrolidone (NMP) were purchased from Sinopharm Chemical Reagent Corp. Dimethylsulfoxide (DMSO, 99.95%) was purchased from Alfa Aesar. Bismuth (Bi) chunks were purchased from ZhongNuoXinCai Technology Co., LTD., Beijing. Polyvinylidene fluoride (PVDF) and deuteroxide ($D_2O$, 99.9%) were purchased from Sigma Aldrich. Carbon paper (CP, Toray TGP-H-060) was purchased from Toray Industries Inc. Acetylene black (AB) was obtained from Kejing Materials Technology Co., LTD. All the chemicals in analytical grade were used for experiments without any purification. All the aqueous solutions were prepared with ultrapure deionized water (18.2 mΩ·cm, Millipore SAS, France).

### 2.2. Synthesis of ultrathin bismuth (Bi) nanosheets

The bulk Bi used in experiments was ground into powder in advance. Firstly, 4 mg/mL metallic Bi powder and 30 mg NaOH were put into 120 mL Ar-saturated IPA solvent operated in a Ar-filled glovebox. Then, the bulk Bi in the sealed bottle was exfoliated by consecutive ultrasonication (60 W, Shanghai Kunshan Corp., 40 kHz) for 30 h to obtain a dark grey suspension of Bi nanosheets. The bath was cooled with ice water and the temperature was kept at room temperature during ultrasonication. The yield and thickness of Bi nanosheets could be further optimized by repeated exfoliation processes. After ultrasonication, the resulting suspension was first centrifuged at 500 rpm for 1 min to remove residual bulk Bi or some thick Bi nanosheets, then the top 2/3 portion of the suspension was carefully collected by pipette. Subsequently, the ultrathin Bi nanosheets were obtained by another centrifugation of the collected supernatant at 5000 rpm for 5 min. After that, the sample was washed with deionized water and ethanol for three times, respectively. The ultrathin Bi nanosheets were then soaked in 500 μL hydrazine hydrate overnight to fully remove the surface oxidization layer. The final products were washed with excess ethanol for several times and dried under vacuum before use. To obtain Bi nanosheets with different sizes (as referred in Fig. S9b), the collected supernatant was centrifugated at 4500 rpm for 3 min. Then, the top 2/3 supernatant was collected as thin nanosheets and the residual was dispersed in ethanol as thick nanosheets.

### 2.3. Characterizations

The morphology and structure of samples were characterized by field-emission scanning electron microscopy (FESEM, FEI Nova-450) and transmission electron microscopy (TEM, JEM-2100). The crystal structures of samples were identified by a powder X-ray diffractometer (XRD, Bruker D8 Advance) with Cu Kα ($\lambda = 1.5406$ Å) irradiation in the range between 20° and 80° at a scanning speed of 10° $in.^{-1}$. Raman spectra were collected with a Horiba JY Evolution spectrometer using a 633 nm laser source. The catalysts before and after electrolysis were analyzed by X-ray photoelectron spectroscopy (XPS) through a PHI-5000 Versa Probe X-ray photoelectron spectrometer with an Al Kα X-ray radiation. For the contact angle measurements, the powder samples were firstly wetted by ethanol and rolled into sheets on aluminum foils, and then dried at 80 °C for 12 h under vacuum, and subsequently measured with an OCA-30 instrument (DataPhysics Instruments GmbH) at room temperature. The UV–Vis absorption spectra were obtained from a Shimadzu UV-2600 spectrophotometer in the range of 200–800 nm (with $BaSO_4$ as reference).

### 2.4. $CO_2$ adsorption measurements

The $CO_2$ adsorption properties of the samples were analyzed on a Quantachrome Autosorb-IQ-2C-TCD-VP instrument. Prior to the experiments, the samples were degassed at 80 °C for 24 h. The $CO_2$ adsorption experiments were proceeded at 25 °C with circulated water cooling and the testing pressure were ranged from 0.05 to 1.00 bar.

### 2.5. Electrochemical measurements

All electrochemical measurements were performed on a CHI-760E electrochemical workstation (ChenHua Instruments, Shanghai) with a standard three-electrode system. Linear sweep voltammetry (LSV) measurements were performed in Ar- or $CO_2$-saturated 0.1 M $KHCO_3$ electrolyte at a scan rate of 20 mV $min^{-1}$ in the voltage range from 0.0 to − 1.2 V (*vs.* RHE). Cyclic voltammetry (CV) method was employed to determine the electrochemical surface area (ECSA). Specifically, CV experiments were performed in 0.1 M $KHCO_3$ electrolyte within a potential range from − 0.3 V to − 0.2 V (*vs.* Ag/AgCl) to ensure non-occurrence of Faradaic processes. The selected scan rates were 5 mV $s^{-1}$, 10 mV $s^{-1}$, 20 mV $s^{-1}$, 30 mV $s^{-1}$, 40 mV $s^{-1}$ and 50 mV $s^{-1}$, respectively. The slope of the linear regression was calculated from the CV curves, which was a plot of capacitive current density ($\Delta j = (j_a - j_c)$, where $j_a$ and $j_c$ are the cathodic and anodic current densities, respectively) at − 0.25 V (*vs.* Ag/AgCl) against the scan rates. The value of ECSA is in proportion to that of the slope. The Electrochemical impedance spectroscopy (EIS) measurements were carried out by applying an AC voltage with 5 mV amplitude in a frequency range from 100 kHz to 100 mHz. The Tafel slope for formate generation was calculated with a plot of overpotential *vs.* the logarithm of $j_{formate}$ (calculated by LSV measurements and $FE_{formate}$).

To prepare the homogeneous pastes of electrocatalysts, active material (ultrathin Bi nanosheets or bulk Bi), AB and PVDF with a weight ratio of 80:10:10 were ground in a mortar for 30 min. Then, the mixture was dissolved in NMP solution to form a slurry. For the fabrication of working electrode, the as-prepared catalyst paste was carefully brushed onto a piece of carbon paper (CP) and dried under vacuum at 80 °C

overnight. The active material loading was ~ 2.0 mg cm$^{-2}$. Before use, The CP should be ultrasonically washed with acetone, water and ethanol. Acetylene black decorated carbon paper (AB/CP) electrode was prepared in the same way without adding Bi nanosheets or bulk Bi. Electrochemical $CO_2$RR was performed in a standard H-type electrochemical cell (Ida Technology Co., LTD., Tianjin), as shown in Scheme S1 at atmospheric pressure and room temperature (25 °C) equipped with a water-cooled condenser. The sealed cell was separated into two compartments with a pre-treated proton exchange membrane (Nafion-117) and each compartment contains 80 mL of 0.1 M $KHCO_3$ aqueous solution with 35 mL of gas headspace. After purged with $CO_2$ gas in both anodic and cathodic compartment for at least 30 min, the pH value of the electrolyte was tested to be ~ 6.8. The electrolytes in both compartments were stirred at 1000 rpm with stirring bars during the $CO_2$RR process. Platinum gauze electrode and Ag/AgCl (saturated KCl) electrode were used as counter electrode and reference electrode, respectively. All the applied potentials are shown as reversible hydrogen electrode (RHE) potentials using the Nernst function as below:

$$E\ (vs.RHE) = E(vs.Ag/AgCl) + 0.1989\ V + 0.059 \times pH \quad (1)$$

### 2.6. Quantitative analysis of gaseous and liquid products

During electrochemical reduction process, a small quantity of gaseous product mixture (200 μL) from headspace was collected using a gastight syringe in 30 min intervals and rapidly injected into the gas sampling loop of a gas chromatograph (GC-7900, Shanghai Techcomp) to quantify the amounts of gaseous products (n in moles). The different components of gas products were separated and detected by a thermal conductivity detector (for $H_2$) and a flame ionization detector (for CO and hydrocarbons) with high-purity argon (Ar) flow as carrier gas. To ensure the accuracy of gas product yields, each quantitative sampling was carried out for two times. After electrolysis process, 0.6 mL electrolyte was collected to quantificationally analyze the amounts of liquid products (n in moles) by nuclear magnetic resonance (NMR, Bruker AV-600). Briefly, 0.6 mL electrolyte was uniformly mixed with 0.1 mL deuterated water ($D_2O$) and 0.1 mL anhydrous dimethyl sulfoxide (DMSO, 99.5%, diluted to 10 ppm (v/v) by water prior to use) as an internal standard. The one-dimensional $^1H$ spectrum was carried out with necessary water peak suppression by a water pre-saturation method. The concentration of formate was determined by the standard curve using various concentrations (0.5, 1.0, 2.0, 5.0 and 10.0 mM) of sodium formate and the internal standard (10 ppm DMSO). The linear relationship between the known formate concentration and relative area (*vs.* 10 ppm DMSO) was made into a standard curve, as shown in Fig. S6b. The Faradaic efficiency (FE) of products can be calculated *via* the following equation:

$$FE = mF \times n/Q = mF \times n/(I \times t) \quad (2)$$

where $F$ is the Faraday constant and $m$ (in number) indicates the required electrons for the generation of one product molecule (*e.g.,* formate, CO, $H_2$ or hydrocarbons, *etc.)*. The amount of charge ($Q$ in coulombs) passed to produce products during a period of reaction time was calculated. $I$ (in amperes) is the constant current at an applied potential and $t$ (in seconds) is the time consumed at the corresponding current during the electrolysis process.

### 2.7. Computational method

The calculations were carried out using DFT method with the Perdew-Burke-Ernzerbof (PBE) form of generalized gradient approximation functional (GGA) [36]. Vienna *ab-initio* simulation package (VASP) was employed [37–40]. The plane wave energy cutoff was set as 400 eV. The Fermi scheme was employed for electron occupancy with an energy smearing of 0.1 eV. The first Brillouin zone was sampled in the Monkhorst–Pack grid [41], using a 3 × 3 × 1 k-point mesh for the surface calculation. The energy (converged to $1.0 \times 10^{-6}$ eV/atom) and force (converged to 0.01 eV/Å) were set as the convergence criterion for geometry optimization. The spin polarization was considered in all calculation.

The (003) and (012) plane surface was obtained by cutting bulk Bi along {003} and {012} direction, respectively. A vacuum layer as large as 12 Å was used along the $c$ direction normal to the surface to avoid periodic interactions. While for the surface edge, a vacuum layer of 15 Å was employed along the $b$ direction of (003) and (012) edges, respectively.

Free energy change from initial states to final states of the reaction is calculated as follows:

$$\Delta G = \Delta E + \Delta ZPE - T\Delta S \quad (3)$$

where $\Delta E$ is the total energy change obtained from DFT calculations, $\Delta ZPE$ is the change in zero-point energy, $T$ is room temperature (298.15 K), and the $\Delta S$ is the change in entropy.

## 3. Results and discussion

### 3.1. Synthesis of ultrathin Bi nanosheets

As illustrated in Fig. 1a, Bi powder was dispersed in an Ar-saturated IPA solution of NaOH, which was subsequently turned into dark grey suspension under energetic ultrasonication, indicating the successful piecemeal exfoliation of bulk Bi to few-layer Bi nanosheets. It is known that layered materials can be exfoliated in proper solvents, according to the following equation:

$$\Delta H_{mix}/V_{mix} = 2(\delta_G - \delta_{sol})^2\varphi/T_{sheet} \quad (4)$$

where $\Delta H_{mix}$ is the enthalpy of mixture, $V_{mix}$ is the volume of mixture, $\delta$ is the square root of surface energy, $\varphi$ is the volume fraction of material, $T_{sheet}$ is the average thickness of nanosheets [42]. The vital function of IPA is to minimize the enthalpy of the mixture, because the surface energy of IPA matches well with that of bulk Bi, thus can widen the layer spacing and weaken the interlayer binding force by ultrasonication. The presence of NaOH also facilitates the exfoliation, owing to the charge transfer between Bi and $Na^+$ that can serve as a driving force to promote the insertion of $Na^+$ into the interlayers. This phenomenon was also emerged in the exfoliation processes of graphene, bulk $MoS_2$ and antimony (Sb) with the presence of NaOH [43]. With the aid of vigorous ultrasonication, enough energy can be delivered to break the *van der Waals* interactions between Bi atomic layers to form ultrathin nanosheets.

The structural features of the samples were characterized and compared. The scanning electron microscopy (SEM) image in Fig. S1a shows the stacked flakiness morphology of bulk Bi. After exfoliation in NaOH/IPA solution, Bi nanosheets with lateral sizes ranged between ~ 200 nm to several micrometers were obtained, as shown in Fig. S1b. The transmission electron microscopy (TEM) images in Figs. 1b and S1c reveals the ultrathin feature of Bi nanosheets with sub-micron size distribution (Fig. S1d). Through high-resolution TEM (HRTEM) image (Fig. 1c) measured at a selected area in Fig. 1b (marked as point A), the lattice spacing was measured to be 0.395 nm, corresponding to the preferred orientation of Bi (003) plane. Fig. S2 show additional TEM and HRTEM images collected on another two Bi nanosheets. The HRTEM image measured at point B (Fig. S2b) reveals the lattice fringes corresponding to the (110) facets of rhombohedral Bi. The corresponding SAED pattern in the insert of Fig. S2a shows a set of diffraction spots with a six-fold symmetry, of which the zone axis was indexed along [001] direction. Instead, the SAED pattern (the inset of Fig. S2c) and HRTEM image (Fig. S2d) measured at point C exhibit the d-spacings of 0.328 nm and 0.237 nm, corresponding to the (012) and (104) planes of Bi, respectively. These crystalline features are highly consistent with the XRD pattern (Fig. 1g). The thicknesses of few-layer Bi nanosheets determined by atomic force microscopy (AFM) were

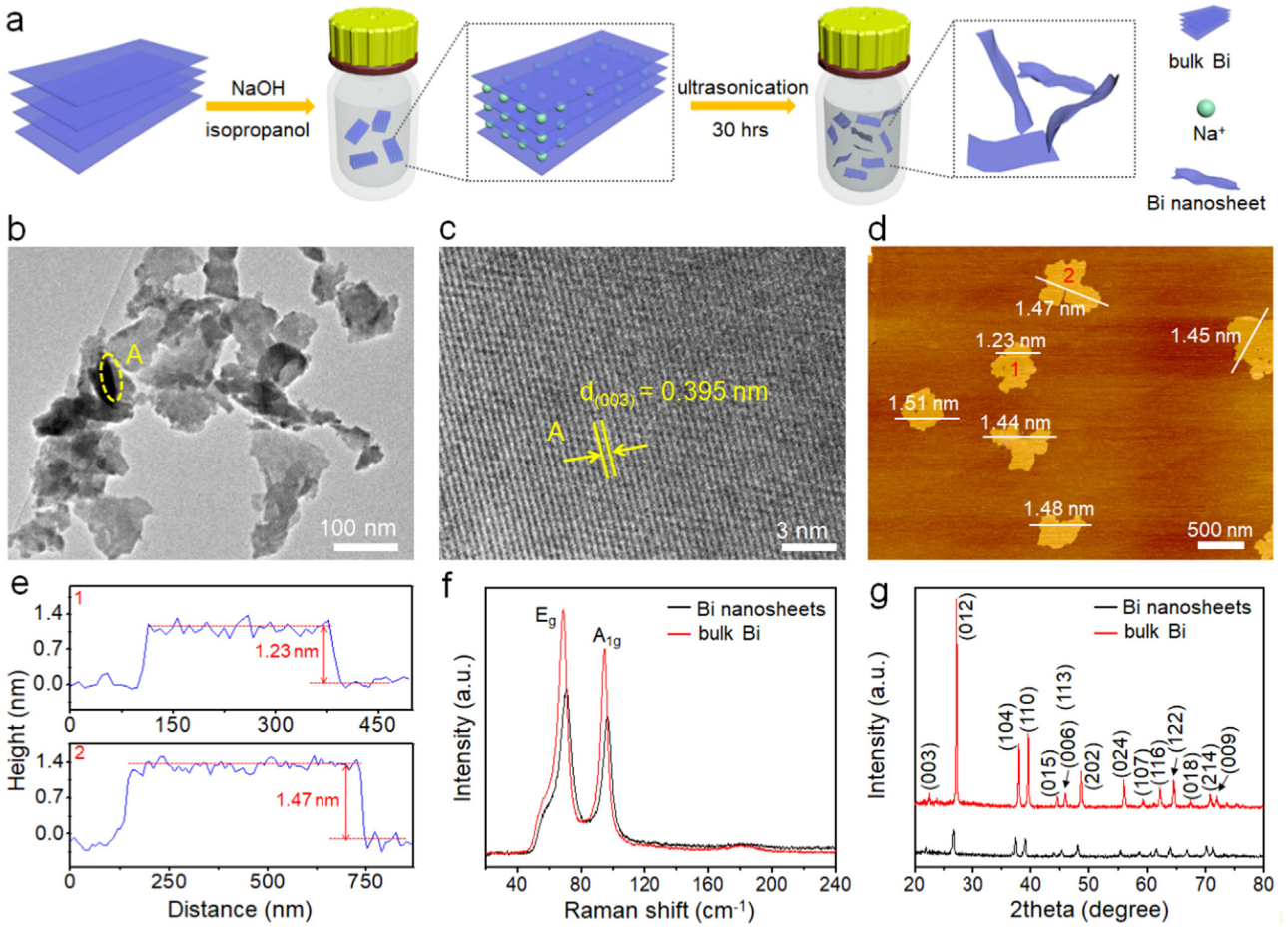


**Fig. 1.** (a) Schematic illustration of the scalable preparation of ultrathin Bi nanosheets *via* a liquid-phase exfoliation process. (b) TEM image and (c) corresponding HRTEM image measured at point A in (b). (d) AFM image and (e) height profiles of few-layer Bi nanosheets. (f) Raman spectra and (g) XRD patterns of Bi nanosheets and bulk Bi.

between 1.23 nm and several nanometers (Fig. 1d and e). The average thickness of the ultrathin Bi nanosheets is between 1.2 and 1.5 nm, corresponding to 3–4 layers of Bi atomic layers, as estimated by comparing with the theoretical atomic layer thickness of Bi (the calculated thickness of Bi monolayer is ~ 0.4 nm). Some thicker Bi nanosheets with the thicknesses less than 3.5 nm were also observed (Fig. S3), confirming the formation of few-layer Bi nanosheets.

The compositions and crystalline structures of Bi nanosheets and bulk Bi were identified by Raman spectroscopy and X-ray diffraction (XRD). The Raman spectrum of Bi nanosheets shows two characteristic peaks of Bi(0) at 71 $cm^{-1}$ ($E_g$ mode) and 98 $cm^{-1}$ ($A_{1g}$ mode), while no peak of oxidation phases (α-$Bi_2O_3$ or β-$Bi_2O_3$) was observed (Fig. 1f). Compared to bulk Bi, both $E_g$ and $A_{1g}$ peaks of Bi nanosheets blue-shifted to higher wavenumbers, accompanied with the decrease of peak intensities and the broadening of full-width-at-half maximums (FWHMs), suggesting the decrease in the degree of long range order induced by exfoliation [44]. The XRD pattern of Bi nanosheets (Fig. 1g) is consistent with rhombohedral Bi (JCPDS no. 44-1246) and shows no indication of oxidized Bi components. Compared to bulk Bi, the diffraction peaks of Bi nanosheets become weaker and show a downshift of diffraction angles, suggesting enlarged interlayer spacings and decreased crystalline periodicity. Furthermore, the UV–vis absorption spectra of Bi nanosheets and bulk Bi are shown in Fig. S4. Unlike the metallic bulk Bi, Bi nanosheets show an absorption band at around 281 nm due to the quantum confinement effect [45,46], further confirming the formation of Bi nanostructure after liquid-exfoliation [47].

### 3.2. Electrochemical $CO_2$ reduction performance

The $CO_2$RR activities of Bi nanosheets and bulk Bi were examined in 0.1 M $KHCO_3$ electrolyte by linear sweep voltammetry (LSV), respectively. The experimental setup is illustrated in Scheme S1 and detailed in the Experimental section of Supporting information. Fig. S5a shows the LSV curves of the samples measured in $CO_2$- or Ar-saturated electrolyte. Clearly, both Bi nanosheets and bulk Bi in $CO_2$-saturated electrolyte (pH = 6.8) exhibit higher current densities than in Ar-saturated electrolyte, indicating that Bi catalysts preferably engender $CO_2$RR rather than HER. Moreover, Bi nanosheets show much higher current density than bulk Bi at the same potentials. These results show that the 2D nanostructure of Bi with abundant active sites is conducive to the electrocatalytic performance. To investigate the catalytic activity of Bi nanosheets, the $CO_2$RR was carried out at different potentials between − 0.5 V and − 1.2 V (*vs.* reversible hydrogen electrode, RHE). Fig. S5b presents the time-resolved current density of Bi nanosheets during an operation period of 4 h. As expected, the current density increased accordingly when the applied potential became more negative (Fig. 2a). After testing for 4 h, the Faradaic efficiencies of different products were plotted against applied potentials (Fig. 2b). By analyzing with gas chromatograph (GC) and nuclear magnetic resonance (NMR), the product compositions were found to be formate, CO and $H_2$ over the whole potential range (Fig. S6 and Table S2). At a low potential of − 0.5 V (*vs.* RHE), the Faradaic efficiency for formate formation ($FE_{formate}$) was 43.9%, while $H_2$ evolution acted as a considerable competing reaction. When increasing the negative potentials, the $FE_{formate}$ increased rapidly until − 1.1 V (*vs.* RHE), and then started to decline. The Bi nanosheets

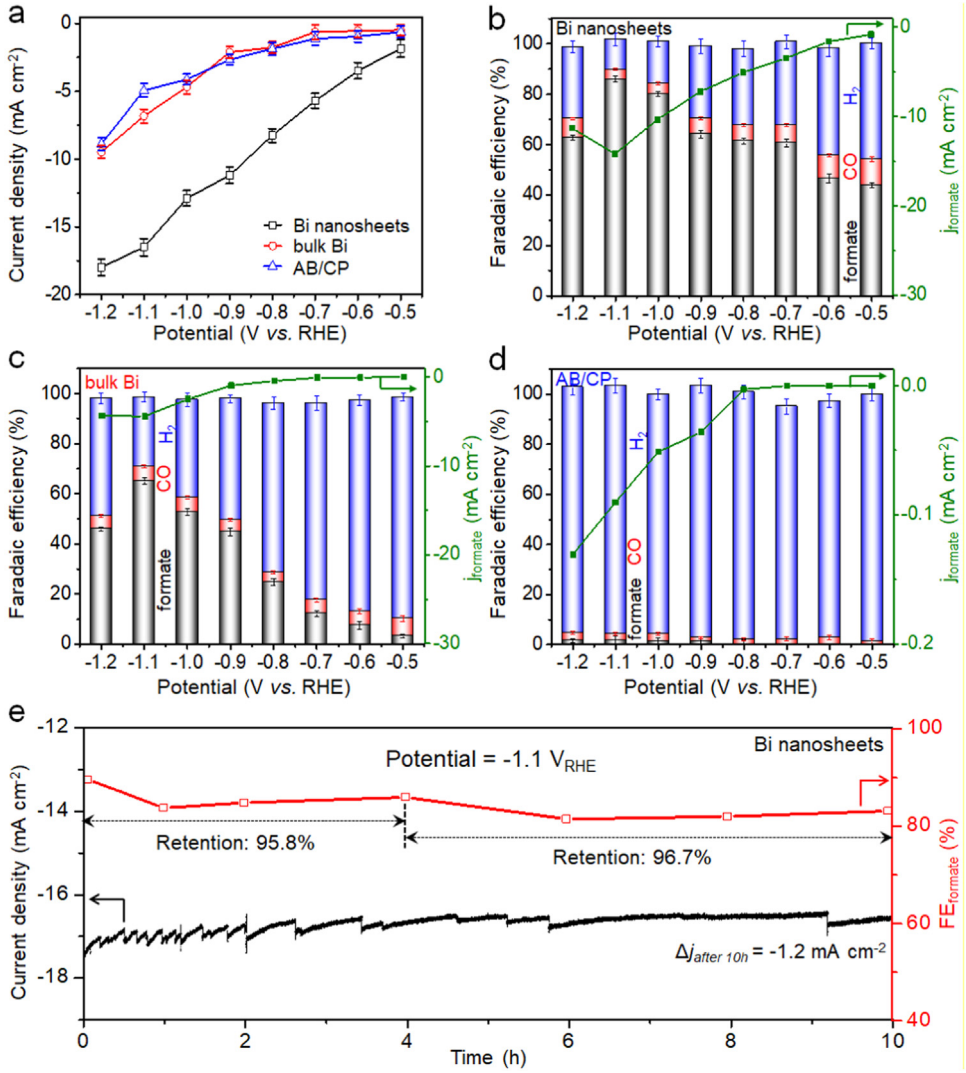


**Fig. 2.** (a) Current densities of Bi nanosheets, bulk Bi and AB/CP within a potential window of − 0.5 to − 1.2 V *vs.* RHE in $CO_2$-saturated 0.1 M $KHCO_3$ aqueous solution. (b–d) Faradaic efficiencies (left Y axes) and partial current densities of formate product (right Y axes) of (b) Bi nanosheets, (c) bulk Bi and (d) AB/CP in $CO_2$-saturated 0.1 M $KHCO_3$ aqueous solution at different applied potentials within 4 h. (e) Current density and $FE_{formate}$ of Bi nanosheets during long-term $CO_2$ electroreduction of 10 h at an applied potential of − 1.1 V (*vs.* RHE). The error bars in (a-d) represent the standard deviations of three independent measurements.

reached a maximum $FE_{formate}$ of 86.0% at − 1.1 V (*vs.* RHE) and delivered a high current density of 16.5 mA $cm^{-2}$. The corresponding total Faradaic efficiency of all carbonaceous compounds ($FE_{C\text{-}total}$) was as high as 90.1%. In contrast, bulk Bi exhibited an optimal $FE_{formate}$ of 64.9% and a current density of 6.8 mA $cm^{-2}$ at − 1.1 V (*vs.* RHE) (Fig. 2a and c), much inferior than Bi nanosheets. Furthermore, the formate partial current densities ($j_{formate}$) of Bi nanosheets and bulk Bi were calculated and plotted against the applied potentials (Fig. 2b, c). The Bi nanosheets delivered a maximum value of $j_{formate}$ = − 14.2 mA $cm^{-2}$ at − 1.1 V (*vs.* RHE), whereas that of bulk Bi is only − 4.5 mA $cm^{-2}$. Due to the combination of high selectivity and large catalytic current density for formate production over a broad potential, Bi nanosheets was highly desirable for $CO_2$ conversion towards formate product. As a common electrocatalyst support, acetylene black decorated carbon paper (AB/CP) was also utilized as another control sample. The AB/CP showed low current densities and little contribution to $CO_2$RR (Fig. 2a and d), because it preferred to generate $H_2$ rather than carbonaceous compounds.

Long-term $CO_2$RR tests were performed to evaluate the durability of Bi nanosheets. During the entire process, $CO_2$ gas was continuously purged into 0.1 M $KHCO_3$ electrolyte to reduce the fluctuation of $CO_2$ concentration and pH value. The Bi nanosheets exhibited remarkable stability after electrolysis of 10 h at − 1.1 V (*vs.* RHE), accompanying with a $FE_{formate}$ retention of 92.6% (Fig. 2e). Moreover, the total current density presented no degradation, confirming the stable performance of Bi nanosheets during long-term testing. The structural integrity of Bi nanosheets after $CO_2$RR process was also investigated. As shown in Fig. S7a and b, the TEM images of Bi nanosheets after $CO_2$RR testing show well-maintained laminar morphology. The XRD pattern, X-ray photoelectron spectroscopy (XPS) and Raman spectrum analysis of Bi nanosheets after $CO_2$RR testing were also performed (Figs. S7c, d and S8). The crystalline structure and the metallic Bi(0) of Bi nanosheets has almost no change.

### 3.3. Discussions

To interpret the enhanced performance of Bi nanosheets, more interfacial and electrochemical characterizations were performed. Fig. 3a and b present the contact angles of Bi nanosheets and bulk Bi with the electrolyte, revealing the superior surface wettability of Bi nanosheets. This may be attributed to the reduced *van der Waals* interactions between Bi interlayers, thus providing a sufficient contact with electrolyte. Electrochemical impedance spectroscopy (EIS) prove that the Bi nanosheets possessed high conductivity and small charge-transfer

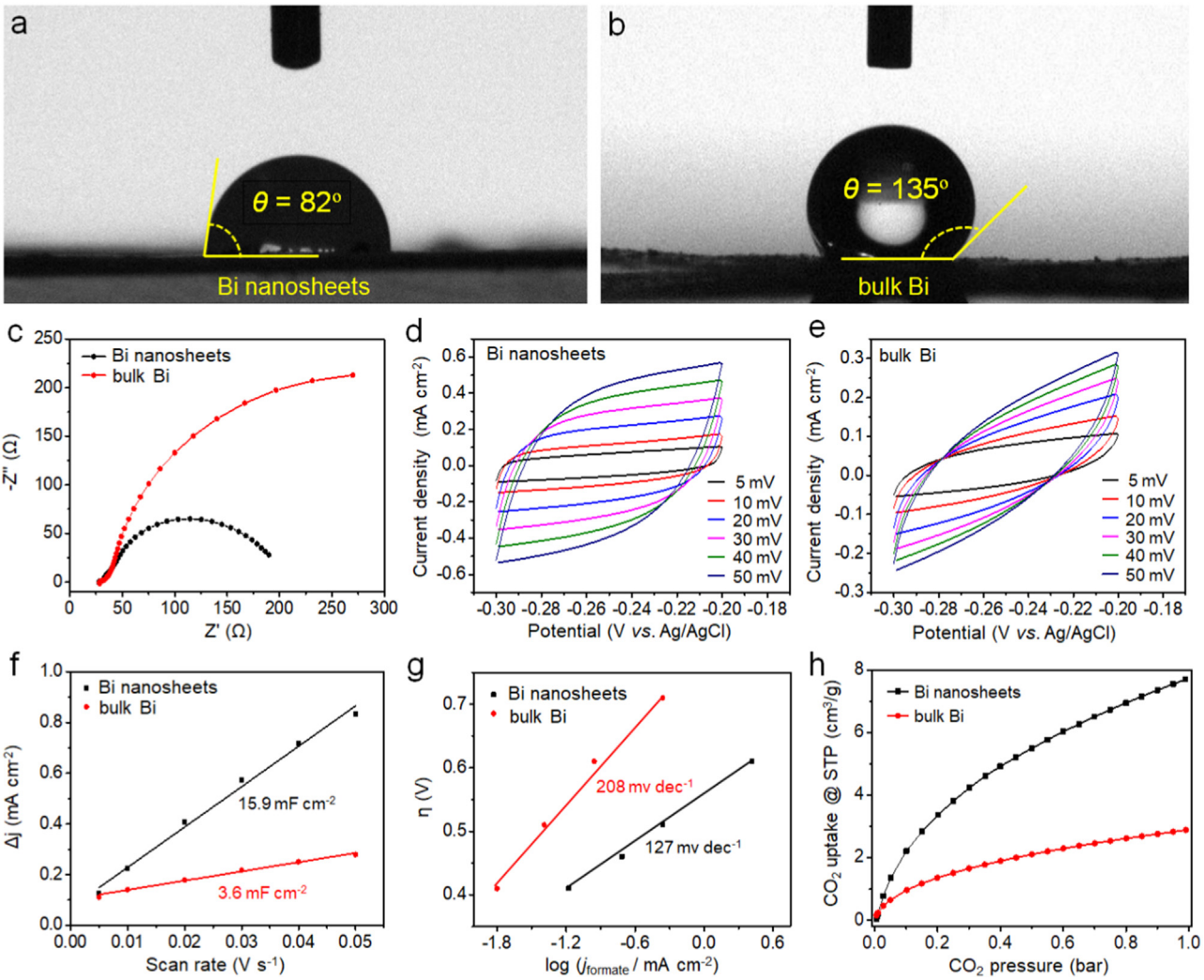


**Fig. 3.** (a, b) Contact angles of Bi nanosheets and bulk Bi with $CO_2$-purged 0.1 M $KHCO_3$ aqueous solution. (c) Nyquist plots of Bi nanosheets and bulk Bi. (d, e) CV curves of (d) Bi nanosheets and (e) bulk Bi measured in Ar-purged 0.1 M $KHCO_3$ aqueous solution. (f) Charging current density differences ($\Delta j$) *vs.* scan rates and (g) Tafel slopes for formate production of Bi nanosheets and bulk Bi. (h) $CO_2$ adsorption isotherms of Bi nanosheets and bulk Bi at 25 °C.

resistance (Fig. 3c), indicating the sufficient interface contact and smooth electron transfer capacity that are crucial for promoting the formation of reaction intermediates in $CO_2$RR. The ECSA and Tafel slopes of the samples were measured to identify the determinants of improved $CO_2$RR activity, such as reaction kinetics, the rate-limiting step and the competitive reaction pathways (Fig. 3d–g). The ECSA of Bi nanosheets (15.9 mF $cm^{-2}$) is 4.4-fold higher than bulk Bi (3.6 mF $cm^{-2}$), indicating the increased active surface area (Fig. 3f). The Tafel plots reveal the enhanced kinetics for $CO_2$RR on Bi nanosheets (Fig. 3g). Bulk Bi exhibits a large Tafel slope (208 mV $dec^{-1}$), suggesting the inferior $CO_2$ activation on bulk surface. The Tafel slope of Bi nanosheets (127 mV $dec^{-1}$) is much lower, indicating the favorable $CO_2$ adsorption resulting in enhanced catalytic activity. Meanwhile, the larger $CO_2$ uptake capacity of Bi nanosheets at room temperature (Fig. 3h) further demonstrates the faster reaction kinetics of 2D Bi catalyst for $CO_2$RR. The improved electrocatalytic performance induced from 2D structure is also evidenced by the positive shift of onset potential (Fig. S5a). However, the Tafel slopes of both bulk Bi and Bi nanosheets deviate from the expected value of 118 mV $dec^{-1}$, indicating that the rate limiting step of both samples is different from the involvement of an initial $1e^-$ transfer.

Fig. S9a and Table S1 summarized the performance comparison of Bi nanosheets with other typical electrocatalysts in literatures (*e.g.*, $d^{10}$ transition metals, alloys and 2D materials) [28–35], indicating that the Bi nanosheets have good prospects for $CO_2$RR with favorable catalytic activity and selectivity. To understand the origins of enhanced performance, it is necessary to gain a fundamental insight into the role of 2D nanostructure through theoretical simulations. As confirmed by previous studies, the rich active edge sites on 2D materials are responsible for the enhanced $CO_2$RR activity [48–50]. To verify this statement, Bi nanosheets with different thicknesses were obtained by centrifugation and loaded on CP to obtain the polarization curves in $CO_2$-purged 0.1 M $KHCO_3$ solution. As shown in Fig. S9b, the $I_{mass}$ (current normalized by the mass loading of Bi nanosheets on CP) of thinner Bi nanosheets is higher than that of the thicker ones. Since the total edge length is inversely proportional to the size of 2D nanosheets when the mass loading is constant [34], the positive relationship between $I_{mass}$ and the edge length of Bi nanosheets confirms that edge sites are actually more active than facet sites. Accordingly, we investigated the different effects of increased facet sites and edge sites on the catalytic activity of Bi nanosheets. The possible reaction pathway went through the formation of *OCOH intermediate, which was found to be the energetically favorable choice for formate production in terms of reaction free energetics [14,51]. The elementary steps are listed below:

$$CO_2\ (sol.) \rightarrow *CO_2\ (ads.) \quad (5)$$

$$*CO_2\ (ads.) + e^- + H^+ \rightarrow *OCOH\ (ads.) \quad (6)$$

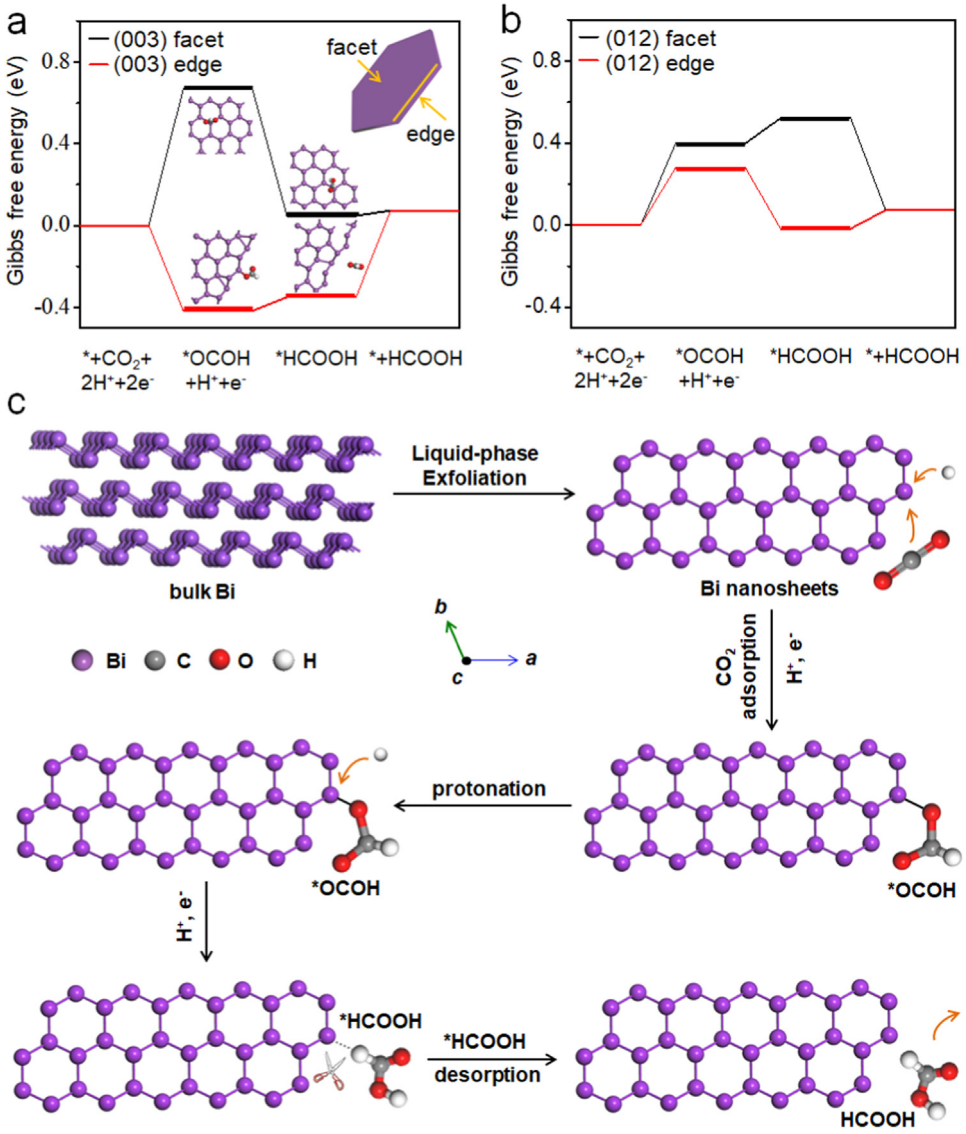


**Fig. 4.** DFT-calculated $\Delta G$ in the reaction pathways of $CO_2$ conversion into formate from the facet sites and edge sites of (a) (003) plane and (b) (012) plane on Bi. (c) Schematic illustration of the mechanism for selective formate formation on Bi nanosheets.

$$*OCOH\ (ads.) + H^+ + e^- \rightarrow *HCOOH\ (ads.) \quad (7)$$

$$*HCOOH\ (ads.) \rightarrow HCOOH\ (sol.) \quad (8)$$

Through density functional theory (DFT) method, the Gibbs free energy changes ($\Delta G$) on facet sites and edge sites for HCOOH generation were calculated (Fig. 4a). On the close-packed surface of (003) plane, the required ΔG for Bi edge sites to convert adsorbed $CO_2$ molecule into *OCOH is − 0.41 eV, much lower than that of facet ones (0.67 eV), indicating the higher activity of edge sites. The calculations revealed that the reaction may be limited by the first proton-coupled electron-transfer step (PES) for bulk Bi, in which facet sites are dominant. In contrast, Bi nanosheets with rich edge sites could perform a highly exothermic and spontaneous process for *OCOH formation. For comparison, we also calculated the Gibbs free energy changes on the (012) plane, which shows the strongest peak intensity in the XRD patterns. As shown in Fig. 4b, the DFT calculation results of (012) plane shows the similar thermodynamic preference to those of (003) plane towards HCOOH generation. However, the calculated $\Delta G$ levels of (012) plane are higher than those of (003) plane, indicating the lower catalytic activity, especially the edge sites. Due to the decreased activation energy barrier of PES, Bi nanosheets exhibit energetically thermodynamic preference for *OCOH formation. As illustrated in Fig. 4c, the *OCOH intermediate was easily formed on the edge site of Bi nanosheets to form a stable configuration. Through the following proton/electron transfer, HCOOH molecule was obtained after the formation and desorption of *HCOOH intermediate. In result, the reaction pathway towards HCOOH generation becomes a priority, resulting in rapid formation of intermediates and high selectivity for formate production.

## 4. Conclusions

In summary, we have developed an efficient liquid-phase exfoliation method to prepare ultrathin Bi nanosheets for electrochemical $CO_2$RR. Compared to bulk Bi, the ultrathin feature, larger ECSA, lower Tafel slope and more exposed edge sites of Bi nanosheets are the reasons of improved catalytic activity. As confirmed by DFT calculations, the formation of *OCOH intermediate was more favorable on edge sites rather than on facet ones due to the more negative reaction free energetics. In result, the ultrathin Bi nanosheets reached much superior activity, selectivity and stability for formate production to bulk Bi. This study suggests the significant potential of 2D nanostructured metals for

highly-efficient and long-life electrocatalytic $CO_2$ conversion.

## Acknowledgements

This work is supported by National Key R&D Program of China (2017YFA0208200, 2016YFB0700600, 2015CB659300), Projects of NSFC (21872069, 51761135104, 21573108), Natural Science Foundation of Jiangsu Province (BK20180008), High-Level Entrepreneurial and Innovative Talents Program of Jiangsu Province, and the Fundamental Research Funds for the Central Universities of China (020514380146).

## Appendix A. Supplementary material

Supplementary data associated with this article can be found in the online version at doi:10.1016/j.nanoen.2018.09.053.

## References

[1] S. Solomon, G.K. Plattner, R. Knutti, P. Friedlingstein, Proc. Natl. Acad. Sci. USA 106 (2009) 1704–1709.
[2] V.K. Arora, J.F. Scinocca, G.J. Boer, J.R. Christian, K.L. Denman, G.M. Flato, V.V. Kharin, W.G. Lee, W.J. Merryfield, Geophys. Res. Lett. 38 (2011) 387.
[3] D.D. Zhu, J.L. Liu, S.Z. Qiao, Adv. Mater. 28 (2016) 3423–3452.
[4] Y. Hori, Mod. Asp. Electrochem. 42 (2008) 89–189.
[5] J.L. Qiao, Y.Y. Liu, F. Hong, J.J. Zhang, Chem. Soc. Rev. 43 (2014) 631–675.
[6] C. Costentin, M. Robert, J. Savéant, Chem. Soc. Rev. 42 (2013) 2423–2436.
[7] J.H. Wu, Y. Huang, W. Ye, Y.G. Li, Adv. Sci. 4 (2017) 1700194.
[8] B. Kumar, V. Atla, J.P. Brian, S. Kumari, T.Q. nNguyen, M. Sunkara, J.M. Spurgeon, Angew. Chem. Int. Ed. 56 (2017) 3645–3649.
[9] X.W. Yu, P.G. Pickup, J. Power Sources 182 (2008) 124–132.
[10] N.S. Spinner, J.A. Vega, W.E. Mustain, Catal. Sci. Technol. 2 (2012) 19–28.
[11] Y. Kwon, J. Lee, Electrocatalysis 1 (2010) 108–115.
[12] H.R.M. Jhong, S.C. Ma, P.J. Kenis, Curr. Opin. Chem. Eng. 2 (2013) 191–199.
[13] W.J. Zhang, Y. Hu, L.B. Ma, G.Y. Zhu, Y.R. Wang, X.L. Xue, R.P. Chen, S.Y. Yang, Z. Jin, Adv. Sci. 5 (2017) 1700275.
[14] J.H. Koh, D.H. Won, T. Eom, N. Kim, K.D. Jung, H. Kim, Y.J. Hwang, B.K. Min, ACS Catal. 7 (2017) 5071–5077.
[15] R. Mohan, Nat. Chem. 2 (2010) 336.
[16] J. Greeley, T.F. Jaramillo, J. Bonde, I. Chorkendorff, J.K. Nørskov, Nat. Mater. 5 (2006) 909–913.
[17] J.L. DiMeglio, J. Rosenthal, J. Am. Chem. Soc. 135 (2013) 8798–8801.
[18] J. Medina-Ramos, J.L. DiMeglio, J. Rosenthal, J. Am. Chem. Soc. 136 (2014) 8361–8367.
[19] Z.Y. Zhang, M.F. Chi, G.M. Veith, P.F. Zhang, D.A. Lutterman, J. Rosenthal, S.H. Overbury, S. Dai, H.Y. Zhu, ACS Catal. 6 (2016) (6255–6164).
[20] D.J. Wilhelm, D.R. Simbeck, A.D. Karp, R.L. Dickenson, Fuel Process Technol. 71 (2001) 139.
[21] J. Rosen, G.S. Hutchings, Q. Lu, R.V. Forest, A. Moore, F. Jiao, ACS Catal. 5 (2015) 4586–4591.
[22] F.J. Quan, D. Zhong, H.C. Song, F.L. Jia, L.Z. Zhang, J. Mater. Chem. A 3 (2015) 16409–16413.
[23] S. Gao, X.C. Jiao, Z.T. Sun, W.H. Zhang, Y.F. Sun, C.M. Wang, Q.T. Hu, X.L. Zu, F. Yang, S.Y. Yang, L. Liang, J. Wu, Y. Xie, Angew. Chem. Int. Ed. 55 (2016) 698–702.
[24] S. Gao, Y. Lin, X.C. Jiao, Y.F. Sun, Q.Q. Luo, W.H. Zhang, D.Q. Li, J.L. Yang, Y. Xie, Nature 529 (2016) 68–71.
[25] J.Q. Xu, X.D. Li, W. Liu, Y.F. Sun, Z.Y. Ju, T. Yao, C.M. Wang, H.X. Ju, J.F. Zhu, S.Q. Wei, Y. Xie, Angew. Chem. Int. Ed. 56 (2017) 9121–9125.
[26] M. Asadi, B. Kumar, A. Behranginia, B.A. Rosen, A. Baskin, N. Repnin, D. Pisasale, P. Philips, W. Zhu, R. Haasch, R.F. Klie, P. Král, J. Abiade, A. Salehi-Khojin, Nat. Commun. 5 (2014) 4470.
[27] M. Pumera, Z. Sofer, Adv. Mater. 29 (2017) 1605299.
[28] D.H. Won, C.H. Choi, J. Chung, M.W. Chung, E. Kim, S.I. Woo, ChemSusChem 8 (2015) 3092–3098.
[29] M. Ma, K. Djanashvili, W.A. Smith, Phys. Chem. Chem. Phys. 17 (2015) 20861–20867.
[30] M. Watanabe, M. Shibata, A. Kato, M. Azuma, T. Sakata, J. Electrochem. Soc. 138 (1991) 3382–3389.
[31] R. Kortlever, I. Peters, S. Koper, M.T.M. Koper, ACS Catal. 5 (2015) 3916–3923.
[32] Z. Bitar, A. Fecant, E. Trela-Baudot, S. Chardon-Noblat, D. Pasquier, Appl. Catal. B-Environ. 189 (2016) 172–180.
[33] N. Sreekanth, M. Azeezulla, T.V. Vineesh, K. Sailaja, K.L. Phani, Chem. Commun. 51 (2015) 16061–16064.
[34] F.W. Li, M.Q. Xue, J.Z. Li, X.L. Ma, L. Chen, X.J. Zhang, D.R. Macfarlane, J. Zhang, Angew. Chem. Int. Ed. 129 (2017) 14910–14914.
[35] C.H. Lee, M.W. Kanan, ACS Catal. 5 (2015) 465–469.
[36] J.P. Perdew, K. Burke, M. Ernzerhof, Phys. Rev. Lett. 77 (1996) 3865–3868.
[37] G. Kresse, J. Furthmüller, Comp. Mater. Sci. 6 (1996) 15–50.
[38] G. Kresse, J. Hafner, Phys. Rev. B 47 (1993) 558–561.
[39] G. Kresse, J. Hafner, Phys. Rev. B 49 (1994) 14251–14269.
[40] G. Kresse, J. Furthmüller, Phys. Rev. B 54 (1996) 11169–11186.
[41] H.J. Monkhorst, J.D. Pack, Phys. Rev. B 13 (1976) 5188–5192.
[42] Y. Hernandez, V. Nicolosi, M. Lotya, F.M. Blighe, Z.Y. Sun, S. De, I.T. Mcgovern, B. Holland, M. Byrne, Y.K. Gun'ko, J.J. Boland, P. Niraj, G. Duesberg, S. Krishnamurthy, R. Googhue, J. Hutchison, V. Scardaci, A.C. Ferrari, J.N. Coleman, Nat. Nanotechnol. 3 (2008) 563–568.
[43] J.N. Gu, Z.G. Du, C. Zhang, J.G. Ma, B. Li, S.B. Yang, Adv. Energy Mater. 7 (2017) 1700447.
[44] R. Cusmão, Z. Sofer, D. Bouša, M. Pumera, Angew. Chem. Int. Ed. 129 (2017) 14609–14614.
[45] J. Chen, L.M. Wu, L. Chen, Inorg. Chem. 46 (2007) 586–591.
[46] Y. Wang, J. Chen, L. Chen, Y.B. Chen, L.M. Wu, Cryst. Growth Des. 10 (2010) 1578–1584.
[47] C.Y. Xing, W.C. Huang, Z.J. Xie, J.L. Zhao, D.T. Ma, T.J. Fan, W.Y. Liang, Y.Q. Ge, B.Q. Dong, J.Q. Li, H. Zhang, ACS Photonics 5 (2018) 621–629.
[48] S. Kim, W.J. Dong, S. Gim, W. Sohn, J.Y. Park, C.J. Yoo, H.W. Jang, J. Lee, Nano Energy 39 (2017) 44–52.
[49] T.F. Jaramillo, K.P. Jørgensen, J. Bonde, J.H. Nielsen, S. Horch, I. Chorkendorff, Science 317 (2007) 100–102.
[50] S.B. Liu, H.B. Tao, L. Zeng, Q. Liu, Z.H. Xu, Q.X. Liu, J.L. Luo, J. Am. Chem. Soc. 139 (2017) 2160–2163.
[51] C.X. Zhao, Y.F. Bu, W. Gao, Q. Jiang, J. Phys. Chem. C 121 (2017) 19767–19773.

**Wenjun Zhang** received her B.S. degree in Chemistry from Anhui University, PR China (2015). She is now pursing her Ph.D. degree under the supervision of Prof. Zhong Jin in School of Chemistry and Chemical Engineering, Nanjing University, P.R. China. Her main interest is the design and fabrication nano-catalysts for electrochemical and photo-electrochemical reduction of carbon dioxide.

**Yi Hu** received his B.S. degree in Chemistry from Sichuan University in 2014. He is now pursuing his Ph.D. degree under the supervision of Prof. Zhong Jin in School of Chemistry and Chemical Engineering at Nanjing University. His research interests reside in two-dimensional nanomaterials for electrochemical energy storage and photoelectric conversion.

**Lianbo Ma** is now pursing his Ph.D. degree under the supervision of Prof. Zhong Jin and Jie Liu in School of Chemistry and Chemical Engineering, Nanjing University, P.R. China. His main interest is the design and fabrication nanomaterials for energy storage and electrochemistry.

**Guoyin Zhu** obtained his M.S. degree from Nanjing University of Posts & Telecommunications in 2014. Currently, he is pursuing his Ph.D. degree under the supervision of Prof. Zhong Jin and Jie Liu at Nanjing University. His research is mainly focused on the synthesis of carbonaceous nanomaterials, and their application for energy conversion and storage devices.

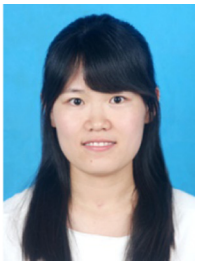

**Xiaolan Xue** received her B.S. degree in School of Chemistry and Chemical Engineering from Shannxi Normal University, PR China (2015). She is now pursing her Ph.D. degree under the supervision of Prof. Zhong Jin in School of Chemistry and Chemical Engineering, Nanjing University, P.R. China. Her research is focused on designing functional materials for rechargeable magnesium batteries and the photocatalytic reduction of dinitrogen.

**Renpeng Chen** graduated from the Northeastern University (2014). Now, he is pursuing his Ph.D. degree under the guidance of Prof. Zhong Jin in School of Chemistry and Chemical Engineering at Nanjing University. His research interest is focused on the synthesis of alloy materials for lithium-ion batteries.

**Peiyang Zhao** received his B.S. degree in Chemistry from Henan Polytechnic University, P.R. China (2015). He is now pursing his M.S. degree under the supervision of Prof. Zhong Jin at School of Chemistry and Chemical Engineering, Nanjing University. His main interest is the design and fabrication of nanomaterials for perovskite solar cells and electrochemical energy storage.

**Songyuan Yang** received his B.S. degree in Chemistry from Nanjing University in 2016. He is now pursing his Ph.D. degree under the supervision of Prof. Zhong Jin and Jie Liu in School of Chemistry and Chemical Engineering, Nanjing University, P.R. China. His main interest is the design and fabrication nano-catalysts for electrochemical and photocatalytic reduction of carbon dioxide.

**Prof. Jing Ma** received her B.S and M.S. in Chemistry from Nanjing University of Science and Technology in 1992 and 1995, respectively, and a Ph.D. in Physical Chemistry from Nanjing University in 1998. She is currently a professor of chemistry at Nanjing University. She is primarily interested in developing electronic structure methods and molecular simulation methods and extending their applications to various functional material systems.

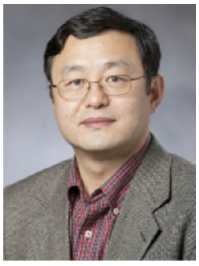

**Prof. Jie Liu** is currently the George B. Geller Professor of Chemistry at Duke University and an adjunct professor of "Thousands Talents" Program at Nanjing University. He earned a B.S. from Shandong University in 1987 and a Ph.D. from Harvard University in 1996. His research interests include the synthesis and chemical functionalization of nanomaterials, nanoelectronic devices, scanning probe microscopy, and carbon nanomaterials. Prof. Liu is a Fellow of the AAAS, APS and RSC.

**Prof. Zhong Jin** received his B.S. (2003) and Ph.D. (2008) in chemistry from Peking University. He worked as a postdoctoral scholar at Rice University and Massachusetts Institute of Technology. Now he is a professor in School of Chemistry and Chemical Engineering at Nanjing University. He leads a research group working on functional nanomaterials and devices for energy conversion and storage.